

# Temporal Variability of Ground Shaking and Stress Drop in Central Italy: A Hint for Fault Healing?

by Dino Bindi, Fabrice Cotton,\* Daniele Spallarossa, Matteo Picozzi, and Eleonora Rivalta

**Abstract** Ground-motion prediction equations (GMPEs) are calibrated to predict the intensity of ground shaking at any given location, based on earthquake magnitude, source-to-site distance, local soil amplifications, and other parameters. GMPEs are generally assumed to be independent of time; however, evidence is increasing that large earthquakes modify the shallow soil conditions and those of the fault zone for months or years. These changes may affect the intensity of shaking and result in time-dependent effects that can potentially be resolved by analyzing between-event residuals (residuals between observed and predicted ground motion for individual earthquakes averaged over all stations). Here, we analyze a data set of about 65,000 recordings for about 1400 earthquakes in the moment magnitude range 2.5–6.5 that occurred in central Italy from 2008 to 2017 to capture the temporal variability of the ground shaking at high frequency. We first compute between-event residuals for each earthquake in the Fourier domain with respect to a GMPE developed *ad hoc* for the analyzed data set. The between-events show large changes after the occurrence of mainshocks such as the 2009  $M_w$  6.3 L'Aquila, the 2016  $M_w$  6.2 Amatrice, and  $M_w$  6.5 Norcia earthquakes. Within the time span of a few months after the mainshocks, the between-event contribution to the ground shaking varies by a factor 7. In particular, we find a large drop in the between-events in the aftermath of the L'Aquila earthquake, followed by a slow positive trend that leads to a recovery interrupted by a new drop at the beginning of 2014. We also quantify the frequency-dependent correlation between the Brune stress drop  $\Delta\sigma$  and the between-events. We find that the temporal changes of  $\Delta\sigma$  resemble those of the between-event residuals; in particular, during the period when the between-events show the positive trend, the average logarithm of  $\Delta\sigma$  increases with an annual rate of 0.19 (i.e., the amplification factor for  $\Delta\sigma$  is 1.56 per year). Breakpoint analysis located a change in the linear trend coefficients of  $\Delta\sigma$  versus time in February 2014, although no large earthquakes occurred at that time. Finally, the temporal variability of  $\Delta\sigma$  mirrors the relative seismic-velocity variations observed in previous studies for the same area and period, suggesting that both crack healing along the main fault system and healing of microcracks distributed at shallow depths throughout the surrounding region might be necessary to explain the wider observations of postearthquake recovery.

*Electronic Supplement:* Maps showing earthquake locations and the locations of stations used in this study, variability with time of the between-event residuals at 10 Hz considering different time windows, time dependency at 10 Hz according to the logarithm of the stress drop, time variability for L'Aquila, Campotosto, and Amatrice–Visso–Norcia earthquakes, and time variability according to the moment magnitude  $M_w$ .

## Introduction

The intensity of seismic shaking at a given site is a function of the earthquake size, style of faulting, source-to-site

distance, and site condition. Ground-motion prediction equations (GMPEs) incorporate these functional dependencies and are time independent, meaning that the intensity of shaking is assumed to be independent of any process affecting the fault zone. However, some observations suggest that shaking intensity changes depending on the timing of earthquakes

\*Also at Institute of Earth and Environmental Science, University of Potsdam, Karl-Liebknecht-Straße 24-25, 14476 Potsdam-Golm, Germany.

within sequences. For example, it has been observed that aftershocks generate lower median ground motion in the high frequencies (e.g., [Boore and Atkinson, 1989](#)), and, therefore, they have been flagged in the recent Next Generation Attenuation-West2 (NGA-West2) strong-motion data set ([Wooddell and Abrahamson, 2014](#)), allowing GMPE developers to treat them differently from mainshocks. Some of the variability in the observed shaking may be explained by variability in the stress drop (e.g., [Wu and Chapman, 2017](#)). Analyzing the NGA-West2 data, [Baltay and Hanks \(2014\)](#) found that average stress drop for mainshocks is 30% larger than the average stress drop for aftershocks.

Identifying repeating deviations from the median model can help distinguish processes that are not modeled but contribute significantly to ground-motion variability. For example, several studies correlated earthquake-specific residuals (also called between-event or interevent residuals) to stress-drop variability (e.g., [Anderson and Lei, 1994](#); [Bindi et al., 2007](#); [Cotton et al., 2013](#); [Ameri et al., 2017](#); [Baltay et al., 2017](#); [Bindi et al., 2017](#); [Oth et al., 2017](#); [Trugman and Shearer, 2018](#)). Therefore, the presence of any temporal pattern in the distribution of residuals can be used as diagnostic of time-dependent fault or medium properties and ultimately help in understanding how nonstationary processes, such as protracted seismic sequences or the long precursory phase of large earthquakes, affect ground motion. For example, [Socquet et al. \(2016\)](#) and [Piña-Valdés et al. \(2018\)](#), in discussing the ground-shaking time dependencies observed during the 2014 Iquique subduction sequence, suggested that the temporal changes in the between-event residuals were associated with aseismic slip around the rupture area.

Here, we take advantage of a large data set from central Italy to investigate the temporal changes of the between-event residuals and their link with the stress-drop  $\Delta\sigma$  variability. The data set includes about 1400 earthquakes in the magnitude range 2.5–6.5, belonging to the main sequences of the last 10 yrs, that is, the 2009 L'Aquila ([Chiaraluca et al., 2011](#)) and the 2016–2017 Amatrice–Visso–Norcia ([Chiaraluca et al., 2017](#)) sequences. About 60 earthquakes occurred in the area of the 2013–2014 Gubbio swarm ([De Gori et al., 2015](#)) are included as well. We first calibrate an *ad hoc* GMPE for the Fourier amplitude spectra and we evaluate the between-event residuals at different frequencies. Then, the between-events are used as an exploratory tool to detect event-dependent temporal changes in the ground shaking, and we conclude presenting the temporal variability of  $\Delta\sigma$ .

## Data

In this study, we analyze about 65,000 recordings (for each component of motion) from 1400 earthquakes recorded by 340 stations installed in central Italy (Fig. 1 and © Fig. S1, in the electronic supplement to this article). The earthquakes cover the magnitude range from 2.5 to 6.5, and hypocentral distances from 10 to 180 km are considered. The data set includes the main sequences that occurred in the area in the

last 10 yrs, namely the 2009  $M_w$  6.3 L'Aquila (indicated as  $e_1$  in Fig. 1), the 2016  $M_w$  6.1 Amatrice ( $e_2$  in Fig. 1), the 2016  $M_w$  6.1 Visso ( $e_4$  in Fig. 1), and the 2016  $M_w$  6.5 Norcia ( $e_3$  in Fig. 1) (for a map with the time evolution of the events, see © Fig. S2). Following [Bindi et al. \(2018\)](#), in this study we consider the moment magnitude from the Geofon catalog for all events with  $M_w \geq 5.7$  except for the 2009 L'Aquila mainshock, for which we use the Global Centroid Moment Tensor value because the Geofon solution is not available (see [Data and Resources](#)). The data set also includes recordings from 59 earthquakes with magnitude larger than 2.5 that occurred in the area of the 2013–2014 Gubbio swarm; a complete description of the swarm is given by [De Gori et al. \(2015\)](#) and [Valoroso et al. \(2017\)](#). The station distribution is shown in © Figure S1.

We analyze the Fourier amplitude spectra (FAS) of *S*-wave windows band-pass filtered with a variable high-pass corner frequency depending on the signal-to-noise ratio. The Butterworth high-pass corner varies in the 0.05–0.4 Hz range, whereas the low pass one was fixed to 40 Hz. The FAS are smoothed using the [Konno and Ohmachi \(1998\)](#) algorithm (the smoothing parameter  $b$  was set to 40). Details about the data selection and processing are provided by [Pacor et al. \(2016\)](#) and [Bindi et al. \(2017\)](#).

## Source Parameters

For each earthquake, we consider the source parameter (i.e., stress drop and seismic moment) derived by [Bindi et al. \(2017\)](#), using a generalized inversion technique (GIT). In the GIT approach (e.g., [Castro et al., 1990](#); [Oth et al., 2011](#)), the spectral values of a set of earthquakes recorded by a network of stations are simultaneously inverted to isolate the contribution of source, propagation, and site effects. The GIT approach exploits the redundancy of information (i.e., the same earthquake is recorded at several stations located at different distances, and several earthquakes are recorded at the same station) to set up an overdetermined system of equations solved in a least-squares sense. To remove unresolved degrees of freedom which generate trade-offs among different components of the solution, some constraints are applied, such as the choice of a reference distance at which the attenuation is assumed to be one and a reference site condition (i.e., one or more stations for which site amplification is assumed to be known). In this study, we use the results of [Bindi et al. \(2018\)](#), who applied a nonparametric GIT inversion whenever any *a priori* seismological models for source and attenuation were adopted during the GIT inversion. To estimate the seismic moment and the corner frequency for each earthquake, the resulting nonparametric source spectra were fit to a [Brune \(1970\)](#) source model, which assumes a circular fault with uniform stress drop. In [Bindi et al. \(2018\)](#), the source fit was performed, allowing a deviation of the high-frequency acceleration spectral level from a constant value, as predicted by the Brune model. The high-frequency slope of the source spectrum is referred to as  $k_{\text{source}}$ . Given the seismic moment

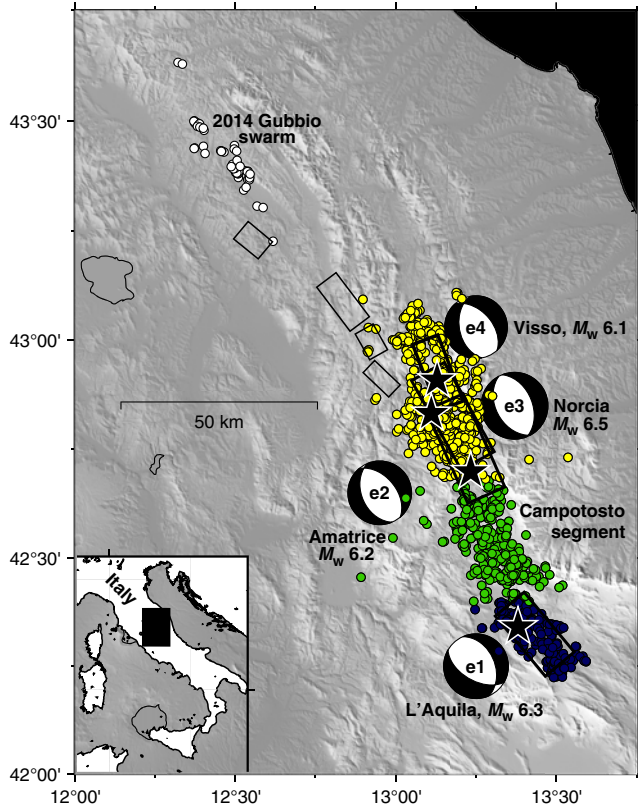


**Figure 1.** Map of earthquake epicenters (circles) analyzed in this study (see [Data and Resources](#)). Circles are filled according to the latitude of the epicenter, assuming arbitrary thresholds at latitudes  $42.4^\circ$  and  $42.68^\circ$ . A few earthquakes belonging to the 2014 Gubbio swarm are also included. The focal mechanisms of earthquakes with magnitude larger than 6 are shown as focal mechanism plots taken from Geofon and from the Global Centroid Moment Tensor catalogs (see [Data and Resources](#)). The rectangles depict the surface projection of the faults as given in [Luzi et al. \(2016\)](#). The color version of this figure is available only in the electronic edition.

and the corner frequency, the stress drop was computed following [Eshelby \(1957\)](#) and [Keilis-Borok \(1959\)](#).

The source parameters are shown in Figure 2, in terms of scaling between  $\Delta\sigma$ ,  $M_w$ , and hypocentral depth. Most of the considered depths, including those of the mainshocks, are located between 5 and 10 km. The stress drop tends to increase with depth and has a strong magnitude dependence ([Pacor et al., 2016](#); [Bindi et al., 2017](#)). The mainshocks have the largest  $\Delta\sigma$  around 10 MPa. The overall  $\Delta\sigma$  variability covers almost 3 orders of magnitude. The procedure followed in this study to estimate the uncertainties on  $\Delta\sigma$  is described in the [Ⓔ](#) electronic supplement.

### Ground-Motion Model

In this study, we describe the FAS( $f, R$ ) at frequency  $f$  of  $S$  waves recorded at hypocentral distance  $R$  with the following seismological model:

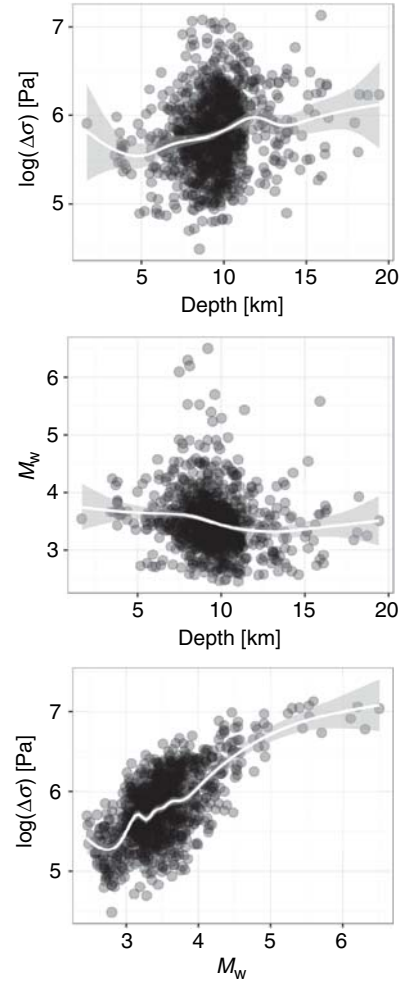


**Figure 2.** Scaling relationships between stress drop  $\Delta\sigma$ , hypocentral depth, and moment magnitude  $M_w$  for the earthquakes analyzed in this study ([Bindi et al., 2018](#)). The trend lines are estimated through a local regression (Loess) performed using the `ggplot2` package in R ([Wickham, 2009](#)).

$$\text{FAS}(f, R) = S(f) \times P(f, R) \times Z(f)$$

$$= K \frac{M_0 f^2}{1 + (\frac{f}{f_c})^2} \times \frac{1}{R^n} \exp\left(-\frac{\pi f R}{Q\beta}\right) \times Z(f), \quad (1)$$

in which the acceleration source spectra  $S(f)$  is parameterized considering an  $\omega$ -square model ([Aki, 1967](#)) and the spectral attenuation with distance  $P(f, R)$  is controlled by the geometrical spreading exponent  $n$  and the anelastic attenuation, the latter being modeled through the quality factor  $Q(f)$ . In equation (1), the constant  $K$  depends on the density and velocity at the source location, on radiation pattern and free-surface amplification effects, whereas  $Z(f)$  accounts for site amplification effects. We only consider far-field source terms, and extended-source effects are not accounted for. The asymptotic form of the source spectrum is as follows:

$$S(f) \propto \begin{cases} M_0 f_c^2 & \text{if } f \gg f_c \\ M_0 f^2 & \text{if } f \ll f_c \end{cases} \quad (2)$$

The source spectrum depends on two parameters, the seismic moment  $M_0$  and the corner frequency  $f_c$  connected through the stress drop  $\Delta\sigma$  (Brune, 1970; Eshelby, 1957) as follows:

$$\Delta\sigma \propto M_0 d^{-3} \propto M_0 f_c^3, \quad (3)$$

in which  $d$  is the source radius. Considering equation (3), equation (2) can be rewritten as

$$S(f) \propto \begin{cases} M_0^{\frac{1}{3}} \Delta\sigma^{\frac{2}{3}} & \text{if } f \gg f_c \\ M_0 f^2 & \text{if } f \ll f_c \end{cases} \quad (4)$$

If the average stress drop of the analyzed earthquakes is assumed to be constant, the scaling of the source spectrum with the earthquake size is controlled only by the seismic moment (Aki, 1967). Under this assumption and considering a mixed-effect regression (Bates *et al.*, 2015), equations (1) and (4) suggest the following parametric model for FAS( $f, R$ ):

$$\ln(\text{FAS}) = a_1 + a_2 M_w + a_3 \ln(R) + a_4 R + \delta B_e + \delta B_s + \epsilon, \quad (5)$$

in which the moment magnitude  $M_w$  is proportional to  $\log(M_0)$  (Hanks and Kanamori, 1979). In equation (5), the coefficients  $a_i$  are the (frequency-dependent) fixed effects that define the median prediction;  $\delta B_e$  and  $\delta B_s$  are the random effects for the earthquake and station grouping levels, respectively;  $\epsilon$  is the residual distribution. To allow more complex scaling with magnitude, the functional form considered in this study is the following:

$$\begin{aligned} \ln(\text{FAS}) = & e_1 + b_1(M_w - M_{\text{ref}}) + b_2(M - M_{\text{ref}})^2 \\ & + [c_1 + c_2(M_w - M_{\text{ref}})] \ln\left(\frac{R}{R_{\text{ref}}}\right) \\ & + c_3(R - R_{\text{ref}}) + \delta B_e + \delta B_s + \epsilon, \end{aligned} \quad (6)$$

with  $M_{\text{ref}} = 3.5$  and  $R_{\text{ref}} = 1$  km. In equation (6), the fixed-effect coefficients describe the scaling with distance ( $c_1$  and  $c_3$  are connected to the geometrical spreading attenuation and the quality factor, respectively) and with magnitude ( $b_1$  and  $b_2$  are controlling the scaling with the seismic moment). Coefficient  $c_2$  introduces a magnitude dependency in the attenuation with distance, whereas the offset  $e_1$  depends (at high frequency) on source characteristics, such as the average stress drop, among other quantities. The between-event  $\delta B_e$  quantifies the systematic deviation of recordings for the same event, with respect to the median prediction. At high frequencies, the deviation of the stress drop of any earthquakes from the average of the population is expected to contribute to the  $\delta B_e$  residuals, whereas differences in the average radiation pattern among the earth-

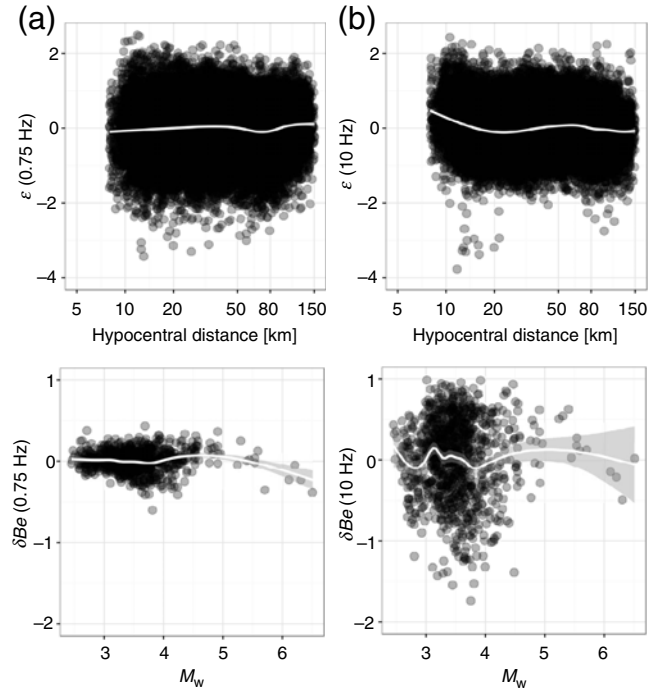


**Figure 3.** Observation minus prediction residuals versus predictor variables for the model in equation (1). The residual  $\epsilon$  versus distance and the between-event  $\delta B_e$  versus moment magnitude  $M_w$  are shown for the regressions performed at (a) 0.75 and (b) 10 Hz.

quakes due to uneven station distribution can contribute to  $\delta B_e$  at low frequency (along with other factors, such as differences in the density and velocity at the source location and errors in the magnitude values). The between-station  $\delta B_s$  random effects, sometimes referred to as  $\delta_{S2S}$ , absorb the frequency-dependent site amplification indicated with  $Z(f)$  in equation (1).

The frequency-dependent coefficients of the model (equation 6) and the standard deviations of  $\delta B_e$ ,  $\delta B_s$ , and  $\epsilon$  are listed in ☹ Table S1. The residuals  $\epsilon$  versus hypocentral distance and  $\delta B_e$  versus magnitude are exemplified in Figure 3 for two frequencies. Over the intervals well constrained by data, the average residuals do not show systematic trends with the predictor variables, but the variability of  $\delta B_e$  increases with frequency (see also ☹ Table S1). Weak trends at short distances (at high frequency) and for large magnitude (at low frequencies) that are not impacting on the analysis performed in this study could be removed by introducing distance and magnitude hinges in equation (5).

### Between-Event Temporal Variability

The temporal trend of the between-event  $\delta B_e$  at 10 Hz is shown in Figure 4, whereas zooms over different time windows are presented in ☹ Figure S3. In addition to the large variability in the aftermath of the mainshock occurrence, the most striking feature in Figure 4 is the positive trend developing from the end of 2009, a few months later than the 6 April 2009 L'Aquila mainshock, to late 2013–early 2014. In

the period from early 2014 to August 2016, when the Amatrice sequence started,  $\delta B_e$  shows a large variability with average value close to zero. When observed at low frequencies (Fig. 4),  $\delta B_e$  shows a weak trend with time. As discussed in the [Ground-Motion Model](#) section,  $\delta B_e$  is expected to absorb, at high frequencies, the effect of the stress-drop variability. Figure 5 shows that the correlation between  $\delta B_e$  and  $\Delta\sigma$  is significant at 10 Hz, whereas the correlation is low at 0.75 Hz. It is worth noting that the mainshocks and the largest aftershocks deviate from the average correlation trend defined by the aftershock population. We ascribe this behavior to the fact that, although  $\Delta\sigma$  varies above 3 orders of magnitude for small events, it is almost constant for earthquakes above magnitude 5. Because GMPEs describe well the average ground shaking generated by the largest magnitudes, their  $\delta B_e$  are distributed close to zero (Fig. 3). The correlation of  $\delta B_e$  with  $\Delta\sigma$  is also highlighted in [Figure S4](#) in which large positive residuals are associated to events with  $\Delta\sigma$  higher than 0.6 MPa (i.e., the population average; [Bindi et al., 2018](#)) whereas earthquakes with lower stress drop have negative residuals. Figure 5 also shows the dependence of  $\delta B_e$  on hypocentral depth. The observed trend is reflecting the  $\Delta\sigma$  dependences on depth, as shown in Figure 2. The degree of correlation measured in terms of Pearson coefficient (Fig. 6) confirms that the correlation is the strongest around 10 Hz. The decrease of correlation toward low frequencies reflects the diminishing importance of  $\Delta\sigma$  in determining the spectral amplitudes at frequencies lower than the corner one, whereas the reduction above 10 Hz suggests that source-related effects other than the stress drop also affect the ground-motion variability at high frequencies. The high-frequency radiations depend on many factors: small-scale slip heterogeneity or slip roughness ([Causse et al., 2010](#)), rupture velocity and slip source function ([Mai et al., 2017](#)), and near-source attenuation ([Purvanche and Anderson, 2003](#)). For example, analyzing a smaller data set, [Bindi et al. \(2017\)](#) found a correlation between  $\delta B_e$  and the slope at high frequency of the acceleration source spectrum.

### Stress-Drop Temporal Variability

The stress-drop variability with time (Fig. 7a) resembles the variability observed for  $\delta B_e$ . If the earthquakes are grouped according to the latitude of their epicenters, as shown in Figure 1, and focusing on the average trend, we observe that

- $\Delta\sigma$  of earthquakes located in the L'Aquila region (Fig. 7b) rapidly diminishes during the first month after the mainshock on 6 April; the recovery starts after about two months (see also Fig. 8a);
- For events located in the Campotosto segment ([Chiaraluca et al., 2011](#); Fig. 7c), the recovery of the logarithm of  $\Delta\sigma$  develops over a time span of 4 yrs, from 2010 to 2013, at an annual rate of 0.17 (i.e., the amplification factor for  $\Delta\sigma$  is 1.5 per year). We recall that the Campotosto segment includes the northernmost termination of the 2009

sequence and the southern tip of the 2016 fault system ([Chiaraluca et al., 2017](#)). In particular, the four events with magnitude larger than 5 that occurred in January 2017 are characterized by large  $\Delta\sigma$  (see Fig. 8), as for the largest aftershocks that occurred over this segment during the 2009 sequence.

- A decrease in  $\Delta\sigma$  is observed at the beginning of 2014, although no large earthquakes occurred at that time. Figure 9 shows the results of a breakpoint analysis ([Bai, 1994](#); [Zeileis et al., 2002, 2003](#)) performed to detect changes in the coefficients of the linear regression with time. The analysis identifies a changepoint within the period 10 February–8 March 2014 across which the slope of the logarithm of  $\Delta\sigma$  with time reduces from  $4.7 \times 10^{-4}$  to  $9.4 \times 10^{-5}$  (the amplification factor per year for  $\Delta\sigma$  reduces from 1.5 to 1). A detailed description of the breakpoint analysis is reported in the [electronic supplement](#). The causes driving this drop are not known. No large earthquakes occurred in the area around February–March 2014; the only notable event is the Gubbio swarm ([Gualandi et al., 2017](#)). At this stage, it is difficult to assess the plausibility of its involvement in the process we are examining here. Possible connections with the seismic and aseismic moment released during the 2013–2014 Gubbio swarm are worth studying in a future work.
- Earthquakes located in the northern group (Fig. 7d) mainly belong to the 2016–2017 Amatrice–Norcia–Visso sequence ([Chiaraluca et al., 2017](#)); also for these events,  $\Delta\sigma$  is larger for the mainshocks and for the aftershocks above magnitude 5.5 ([Figure S5](#)) and decreases after the mainshock occurrence (Fig. 8c). The events that occurred in this area before the 2016–2017 sequence follow the same trends observed for the Campotosto segment.

### Discussions and Conclusions

The between-event residuals  $\delta B_e$  computed for 10 yrs of data in central Italy show significant temporal variability at high frequency (Fig. 4). On the one hand, the time dependency of  $\delta B_e$  implies temporal changes of the ground shaking that could have an impact over the short-term hazard. In the first couple of months,  $\delta B_e$  at 10 Hz varies in the  $-1$  to  $1$  range, roughly (i.e., about a factor 0.7 for spectral amplitudes); after a couple of months from the L'Aquila mainshock, a trend develops with  $\delta B_e$  increasing, on average, from about 0 to 0.8 (i.e., about factor 2 in high-frequency spectral content).

On the other hand, Figure 7 shows that the high-frequency between-event variability resembles the time variability of the stress drop  $\Delta\sigma$ . Temporal variability of  $\Delta\sigma$  has been observed in previous studies. For example, [Abercrombie \(2014\)](#) analyzed 25 earthquakes in three repeating sequences on the San Andreas fault at Parkfield, observing a long-term gradual increase of  $\Delta\sigma$  before the 2004 magnitude 6 earthquake. The values show an immediate decrease after the mainshock occurrence before recovering to previous values. Using a long-term stress-drop catalog, [Chen and](#)

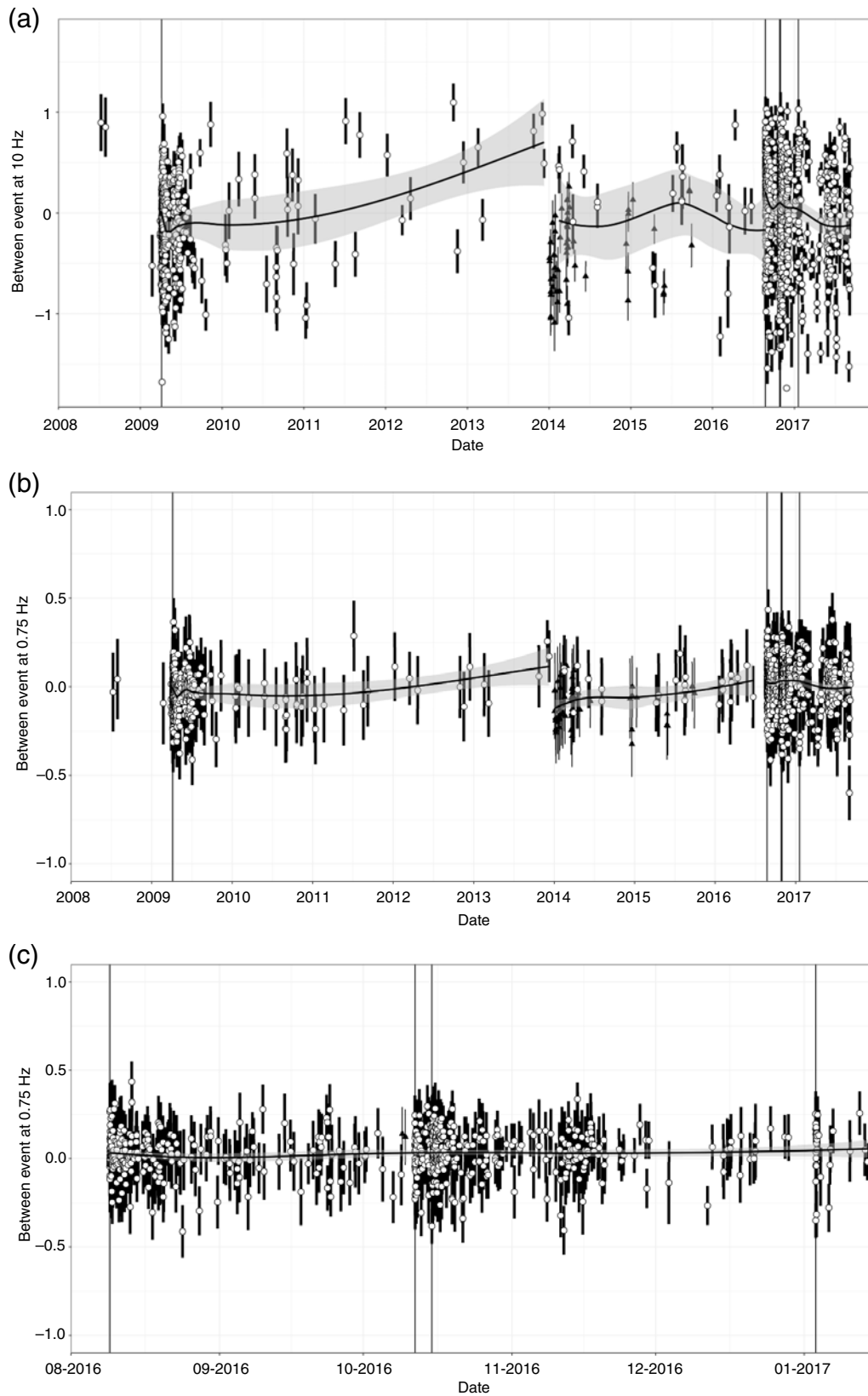


**Figure 4.** (a) Between-event residuals ( $\delta B_e$ ) versus time, at 10 Hz. Earthquakes belonging to the Gubbio swarm (triangles; see Fig. 1) are not considered for evaluating the local-trend analysis; zooms over different time windows are presented in © Figure S3 (available in the electronic supplement to this article). (b) Between-event versus time, at 0.75 Hz; (c) the same as in (b) but zooming over the 2016 sequence. Vertical bars represent the 95% confidence interval for  $\delta B_e$ .

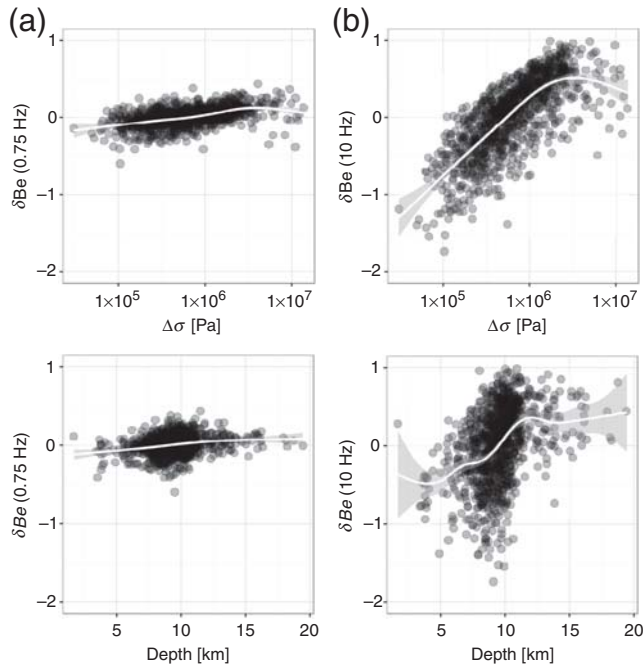


**Figure 5.** Between-event  $\delta B_e$  residuals versus stress drop  $\Delta\sigma$  (top) and hypocentral depth (bottom), considering the results for (a) 0.75 and (b) 10 Hz.

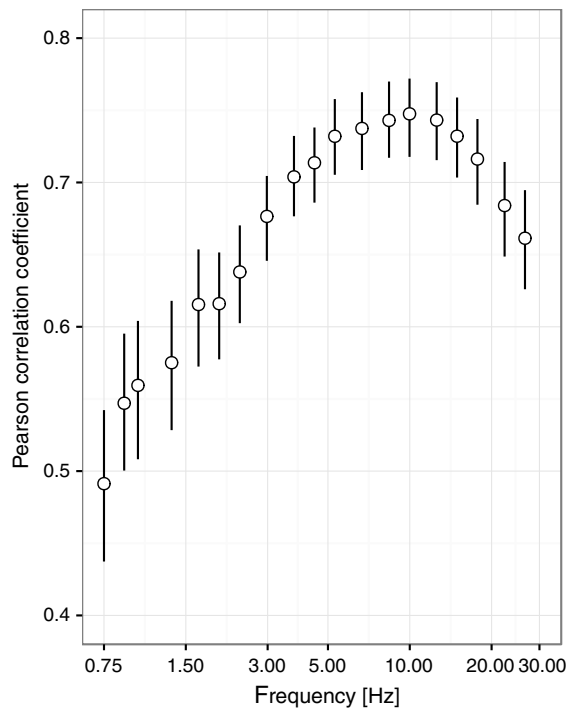


**Figure 6.** Pearson correlation coefficients between  $\Delta\sigma$  and  $\delta B_e$  at different frequencies.

Shearer (2013) found relatively stable long-term average stress drop in southern California, but a slow-increase trend after large mainshocks within the Landers fault zone was also identified, in agreement with a possible long-term fault zone recovery (Li *et al.*, 1998).

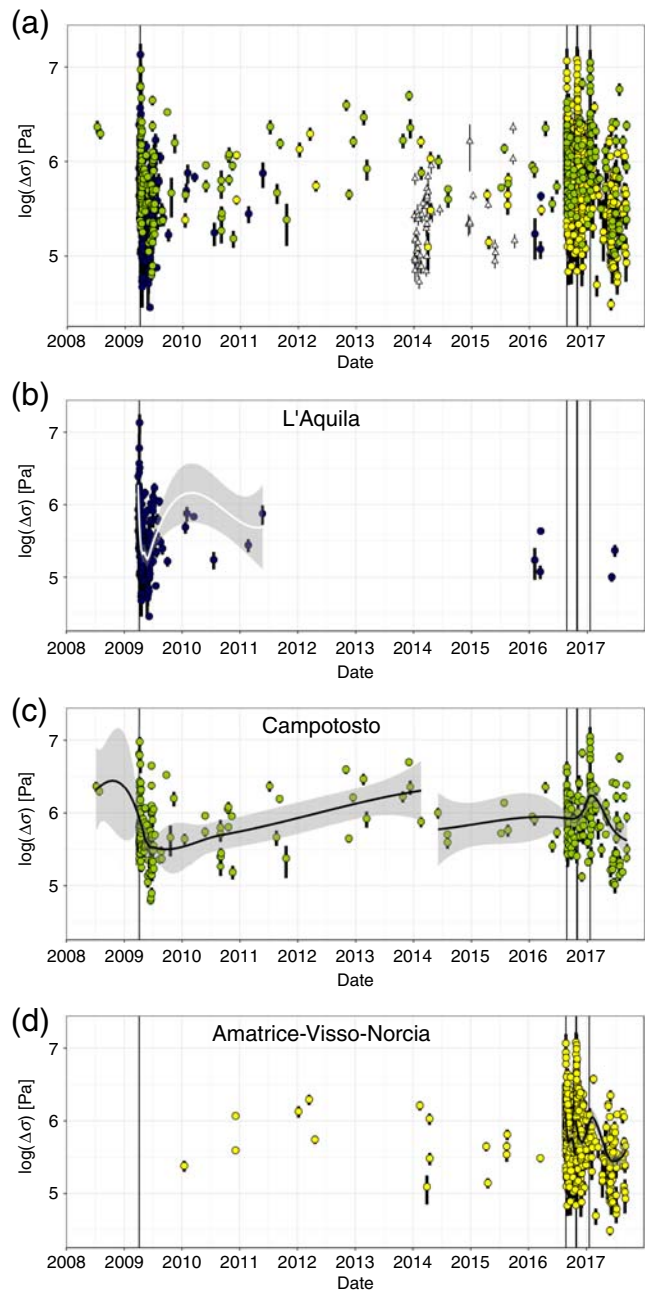


**Figure 7.** Temporal variability of stress drop  $\Delta\sigma$ . (a) Complete distribution of earthquakes; (b) only earthquakes located in proximity to the 2009 L'Aquila mainshock; (c) only earthquakes that occurred in the Campotosto segment; (d) earthquakes that occurred in the area corresponding to the 2016–2017 mainshocks. For the location of the earthquakes in (b)–(d), see Figure 1. Vertical bars represent the 95% confidence interval for  $\Delta\sigma$ . Zooms over different windows are available in Figure 8. The color version of this figure is available only in the electronic edition.

Fault healing has been shown to promote the generation of high-frequency earthquakes both in laboratory experiments and on natural faults (e.g., Marone, 1998; McLaskey *et al.*, 2012; Scuderi *et al.*, 2016). The connection between pore pressure and effective normal stress has been also

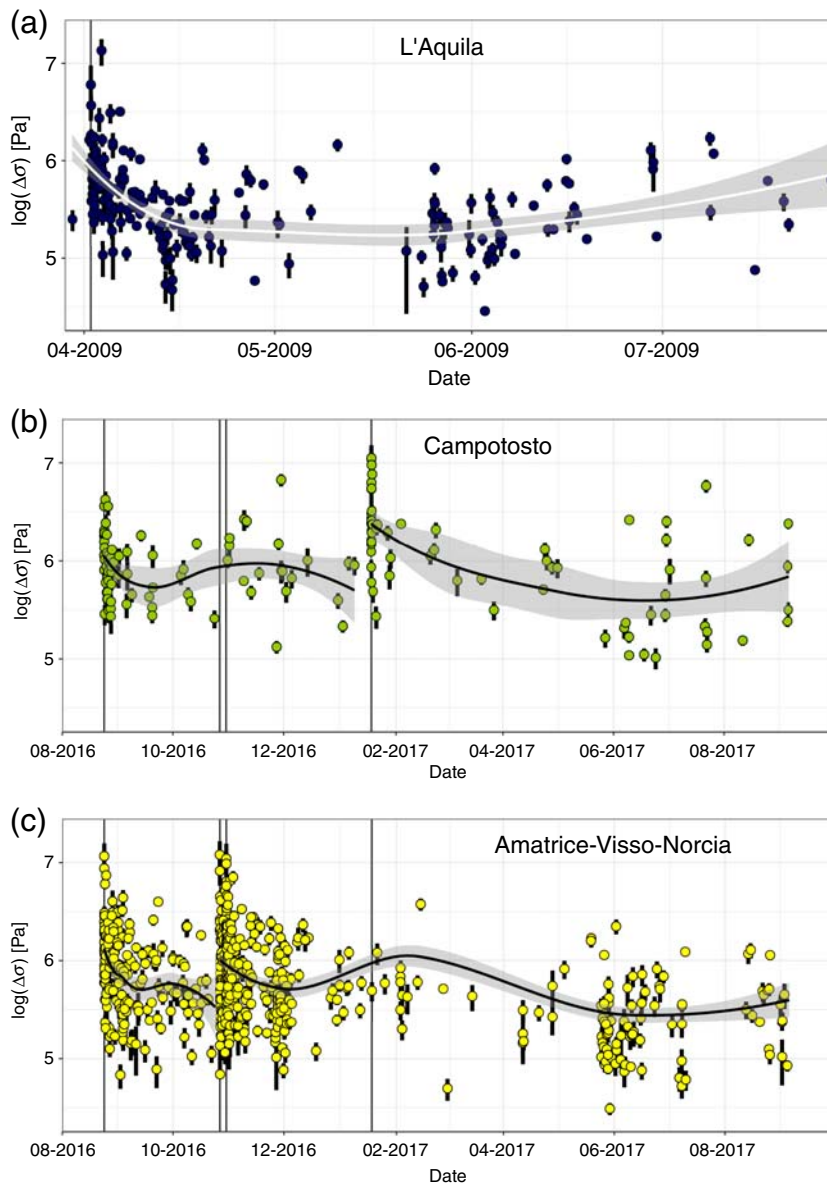


**Figure 8.** Temporal variability of stress drop  $\Delta\sigma$ , considering different zooms of Figure 7. (a) Earthquakes located in proximity to the 2009 L'Aquila mainshock; (b) earthquakes located in the Campotosto segment; (c) earthquakes located in the area corresponding to the 2016–2017 mainshocks. The color version of this figure is available only in the electronic edition.

advocated to explain the time variability of the stress drop. Recently, [Yoshida \*et al.\* \(2017\)](#) analyzed a swarm triggered by the 2011 Tohoku earthquake, evaluating temporal changes in stress drop and  $b$ -value. They discussed the temporal variations of stress drop (very similar patterns to those observed in this study) in terms of changes in the frictional strength due to fluid migration. In central Italy, pore-pressure diffusion due to fluids migration played a role in the preparatory phase of the L'Aquila mainshock (e.g., [Di Luccio \*et al.\* \(2010\)](#)). However, pore-pressure diffusion generally occurs over time scales of weeks to months. Thus, we reckon it is difficult to attribute the variations we observe solely to

migration of fluids or pore pressure that occur over time scales of several years.

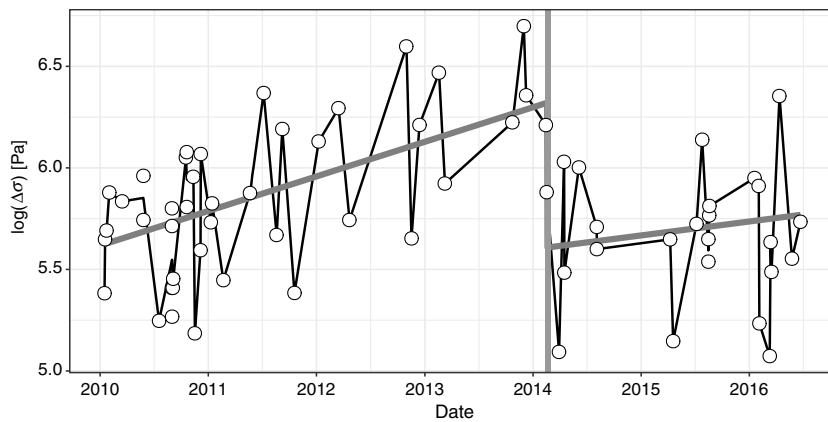
Among other techniques, monitoring changes in seismic velocities has been shown to be effective in detecting fault healing and reloading processes (e.g., [Breguier \*et al.\*, 2008](#); [Chen \*et al.\*, 2010](#)). For example, [Peng and Ben-Zion \(2006\)](#) investigated the temporal variations of seismic velocity along the North Anatolian fault, analyzing repeating earthquake clusters in the aftershock zones of the 1999 İzmit and Düzce earthquakes. The authors observed a sharp seismic-velocity reduction immediately after the Düzce mainshock, followed by a gradual logarithmic-type recovery. They concluded that the temporal changes of material properties occur in the topmost portion of the crust and, although the change is more prominent at stations located close to recently ruptured fault zones, it is not limited to the immediate vicinity of the fault zone. In central Italy, [Soldati \*et al.\* \(2015\)](#) computed the relative velocity variation from cross correlations of noise data over the period 2008–2012, including the 2009 L'Aquila mainshock. The temporal variation obtained for the relative velocity (reproduced in Fig. 10) has a trend very similar to the stress drop: an abrupt coseismic decrease at the time of the mainshock occurrence, followed by an unstable behavior for a few months, and finally, a recovery of the velocity (see also in Fig. 7c). Regarding the spatial distribution of the coseismic-velocity drop, [Soldati \*et al.\* \(2015\)](#) compared the velocities changes averaged over a one-month time window selected before and after the mainshock occurrence, excluding the day of the mainshock. They found (see their fig. 5) that the drop was maximum over the area surrounding the L'Aquila epicenter and in the northeast direction from the fault zone, including the Campotosto area.

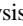
The similarities of the trends observed for the stress drop and for the relative velocity variations suggest that, in agreement with [Heckels \*et al.\* \(2018\)](#), the recovery can be associated both with crack healing along the main fault system and to healing of microcracks distributed at shallow depths throughout the surrounding region.

#### Data and Resources

The R software ([R Development Core Team, 2008](#); <http://www.R-project.org>) has been used in this study to perform the regressions. In particular, the packages `lme4` ([Bates \*et al.\*,](#)





**Figure 9.** Results of the breakpoint analysis (Zeileis *et al.*, 2002, 2003). A change in the linear trend of  $\Delta\sigma$  (gray line) is detected between 10 February and 8 March 2014 (vertical gray line). Details of the analysis are reported in the  electronic supplement.

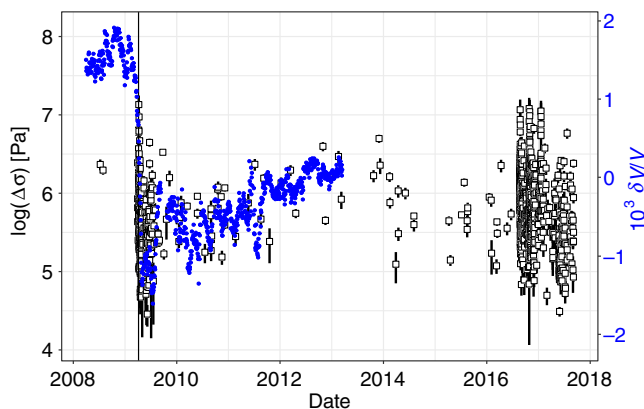


**Figure 10.** Comparison between the relative shear-wave velocity variation computed by Soldati *et al.* (2015) (points) and the  $\Delta\sigma$  (squares) time variability. The color version of this figure is available only in the electronic edition.

2015; <https://cran.r-project.org/web/packages/lme4/news.html>); ggplot (Wickham, 2009; <http://ggplot2.org>); changepoint (Killick and Eckley, 2014; <https://www.jstatsoft.org/article/view/v058i03>); and strucchange (Zeileis *et al.*, 2002; <http://www.jstatsoft.org/v07/i02/>). The waveforms used in this study have been downloaded from the European Integrated Data Archive (EIDA; <https://www.orfeus-eu.org/data/eida/>) and from the Italian Civil Protection (DPC) repository (<http://ran.protezionecivile.it/IT/index.php>). Regarding the permanent networks, we used data from the networks with the International Federation of Digital Seismograph Networks (FDSN) code: MN, IV, IT (<http://www.fdsn.org/networks/>). The moment magnitude used in this study for all earthquakes larger than 5.7 have been taken from the Geofon moment tensor catalog (<http://geofon.gfz-potsdam.de/eqinfo/list.php?mode=mt>). Only for L'Aquila mainshock, we used the Global Centroid Moment Tensor (CMT) solution (<http://www>

[.globalcmt.org/CMTsearch.html](http://globalcmt.org/CMTsearch.html)). The earthquake locations are taken from the Istituto Nazionale di Geofisica e Vulcanologia (INGV) bulletin (<http://cnt.rm.ingv.it/inside>). All the websites were last accessed on December 2017. Some of the figures were prepared with Generic Mapping Tool (GMT; Wessel and Smith, 1991).

## Acknowledgments

This study has been partially funded by the H2020 project SERA (Seismology and Earthquake Engineering Research Infrastructure Alliance for Europe). Comments from two anonymous reviewer and Associate Editor M. Chapman are strongly acknowledged. The authors thank L. Zaccarelli, G. Soldati, and L. Faenza for providing their results on velocity variations used in Figure 10.

## References

- Abercrombie, R. E. (2014). Stress drops of repeating earthquakes on the San Andreas fault at Parkfield, *Geophys. Res. Lett.* **41**, 8784–8791, doi: [10.1002/2014GL062079](https://doi.org/10.1002/2014GL062079).
- Aki, K. (1967). Scaling law of seismic spectrum, *J. Geophys. Res.* **72**, 1217–1231.
- Ameri, G., S. Drouet, P. Traversa, D. Bindi, and F. Cotton (2017). Toward an empirical ground motion prediction equation for France: Accounting for regional differences in the source stress parameter, *Bull. Earthq. Eng.* **15**, 4681–4717, doi: [10.1007/s10518-017-0171-1](https://doi.org/10.1007/s10518-017-0171-1).
- Anderson, J. G., and Y. Lei (1994). Nonparametric description of peak acceleration as a function of magnitude, distance, and site in Guerrero, Mexico, *Bull. Seismol. Soc. Am.* **84**, no. 4, 1003–1017.
- Bai, J. (1994). Least squares estimation of a shift in linear processes, *J. Time Anal.* **15**, 453–472.
- Baltay, A., and T. C. Hanks (2014). Understanding the magnitude dependence of PGA and PGV in NGA West 2 data, *Bull. Seismol. Soc. Am.* **104**, 2851–2865, doi: [10.1785/0120130283](https://doi.org/10.1785/0120130283).
- Baltay, A., T. C. Hanks, and N. A. Abrahamson (2017). Uncertainty, variability, and earthquake physics in ground-motion prediction equations, *Bull. Seismol. Soc. Am.* **107**, no. 4, doi: [10.1785/0120160164](https://doi.org/10.1785/0120160164).
- Bates, D., M. Maechler, B. Bolker, and S. Walker (2015). Fitting linear mixed-effects models using lme4, *J. Stat. Softw.* **67**, no. 1, 1–48.
- Bindi, D., S. Parolai, H. Grosser, C. Milkereit, and E. Durukal (2007). Empirical ground-motion prediction equations for northwestern Turkey using the aftershocks of the 1999 Kocaeli earthquake, *Geophys. Res. Lett.* **34**, no. 8, doi: [10.1029/2007GL029222](https://doi.org/10.1029/2007GL029222).
- Bindi, D., D. Spallarossa, and F. Pacor (2017). Between-event and between-station variability observed in the Fourier and response spectra domains: Comparison with seismological models, *Geophys. J. Int.* **210**, doi: [10.1093/gji/ggx217](https://doi.org/10.1093/gji/ggx217).
- Bindi, D., D. Spallarossa, M. Picozzi, D. Scafidi, and F. Cotton (2018). Impact of magnitude selection on aleatory variability associated with ground-motion prediction equations: Part I—Local, energy, and moment magnitude calibration and stress-drop variability in central Italy, *Bull. Seismol. Soc. Am.* **108**, no. 3A, doi: [10.1785/0120170356](https://doi.org/10.1785/0120170356).
- Boore, D. M., and G. M. Atkinson (1989). Spectral scaling of the 1985–1988 Nahanni, Northwest Territories, earthquakes, *Bull. Seismol. Soc. Am.* **79**, 1736–1761.
- Brenguier, F., M. Campillo, C. Hadziioannou, N. M. Shapiro, R. M. Nadeau, and E. Larose (2008). Postseismic relaxation along the San Andreas

- fault at Parkfield from continuous seismological observations, *Science* **321**, 1478–1481, doi: [10.1126/science.1160943](https://doi.org/10.1126/science.1160943).
- Brune, J. N. (1970). Tectonic stress and the spectra of shear waves from earthquakes, *J. Geophys. Res.* **75**, 4997–5009.
- Castro, R. R., J. G. Anderson, and S. K. Singh (1990). Site response, attenuation and source spectra of *S* waves along the Guerrero, Mexico, subduction zone, *Bull. Seismol. Soc. Am.* **80**, 1481–1503.
- Causse, M., F. Cotton, and P. M. Mai (2010). Constraining the roughness degree of slip heterogeneity, *J. Geophys. Res.* **115**, no. B5, doi: [10.1029/2009JB006747](https://doi.org/10.1029/2009JB006747).
- Chen, J. H., B. Froment, Q. Y. Liu, and M. Campillo (2010). Distribution of seismic wave speed changes associated with the 12 May 2008  $M_w$  7.9 Wenchuan earthquake, *Geophys. Res. Lett.* **37**, L18302, doi: [10.1029/2010GL044582](https://doi.org/10.1029/2010GL044582).
- Chen, X., and P. M. Shearer (2013). California foreshock sequences suggest aseismic triggering process, *Geophys. Res. Lett.* **40**, 2602–2607, doi: [10.1002/grl.50444](https://doi.org/10.1002/grl.50444).
- Chiaralucente, L., R. Di Stefano, E. Tinti, L. Scognamiglio, M. Michele, E. Casarotti, M. Cattaneo, P. De Gori, C. Chiarabba, G. Monachesi, et al. (2017). The 2016 central Italy seismic sequence: A first look at the mainshocks, aftershocks, and source models, *Seismol. Res. Lett.* **88**, no. 3, doi: [10.1785/0220160221](https://doi.org/10.1785/0220160221).
- Chiaralucente, L., L. Valoroso, D. Piccinini, R. Di Stefano, and P. De Gori (2011). The anatomy of the 2009 L'Aquila normal fault system (central Italy) imaged by high resolution foreshock and aftershock locations, *J. Geophys. Res.* **116**, no. B12, doi: [10.1029/2011JB008352](https://doi.org/10.1029/2011JB008352).
- Cotton, F., R. Archuleta, and M. Causse (2013). What is sigma of the stress drop? *Seismol. Res. Lett.* **84**, 42–48, doi: [10.1785/0220120087](https://doi.org/10.1785/0220120087).
- De Gori, P., F. P. Lucente, and C. Chiarabba (2015). Stressing of fault patch during seismic swarms in central Apennines, Italy, *Geophys. Res. Lett.* **42**, 2157–2163, doi: [10.1002/2015GL063297](https://doi.org/10.1002/2015GL063297).
- Di Luccio, F., G. Ventura, R. D. Giovambattista, A. Piscini, and F. R. Cinti (2010). Normal faults and thrusts reactivated by deep fluids: The 6 April 2009  $M_w$  6.3 L'Aquila earthquake, central Italy, *J. Geophys. Res.* **115**, no. B06315, doi: [10.1029/2009JB007190](https://doi.org/10.1029/2009JB007190).
- Eshelby, J. D. (1957). The determination of the elastic field of an ellipsoidal inclusion and related problems, *Proc. Math. Phys. Sci.* **441**, 376–396.
- Gualandi, A., C. Nichele, E. Serpelloni, L. Chiaralucente, L. Anderlini, D. Latorre, M. E. Belardinelli, and J.-P. Avouac (2017). Aseismic deformation associated with an earthquake swarm in the northern Apennines (Italy), *Geophys. Res. Lett.* **44**, 7706–7714, doi: [10.1002/2017GL073687](https://doi.org/10.1002/2017GL073687).
- Hanks, T. C., and H. Kanamori (1979). A moment-magnitude scale, *J. Geophys. Res.* **84**, 2348–2350.
- Heckels, R. E. G., M. K. Savage, and J. Townend (2018). Postseismic velocity changes following the 2010  $M_w$  7.1 Darfield earthquake, New Zealand, revealed by ambient seismic field analysis, *Geophys. J. Int.* **213**, no. 2, doi: [10.1093/gji/ggy021](https://doi.org/10.1093/gji/ggy021).
- Keilis-Borok, V. (1959). On the estimation of the displacement in an earthquake source and of source dimension, *Ann. Geofisc.* **12**, 205–214.
- Killick, R., and I. A. Eckley (2014). Changepoint: An R package for change-point analysis, *J. Stat. Softw.* **58**, 1–19.
- Konno, K., and T. Ohmachi (1998). Ground-motion characteristics estimated from spectral ratio between horizontal and vertical components of microtremor, *Bull. Seismol. Soc. Am.* **88**, 228–241.
- Li, Y. G., J. E. Vidale, K. Aki, F. Xu, and T. Burdette (1998). Evidence shallow fault zone strengthening after the 1992  $M$  7.5 Landers, California earthquake, *Science* **279**, no. 5348, 217–219.
- Luzi, L., R. Puglia, E. Russo, and , and ORFEUS WG5 (2016). *Engineering Strong Motion Database, Version 1.0*, Istituto Nazionale di Geofisica e Vulcanologia, Observatories & Research Facilities for European Seismology, doi: [10.13127/ESM](https://doi.org/10.13127/ESM).
- Mai, P. M., M. Galis, K. K. Thingbaijam, J. C. Vyas, and E. M. Dunham (2017). Accounting for fault roughness in pseudo-dynamic ground-motion simulations, *Pure Appl. Geophys.* **174**, 3419–3450.
- Marone, C. (1998). The effect of loading rate on static friction and the rate of fault healing during the earthquake cycle, *Nature* **391**, 69–72.
- McLaskey, G. C., A. M. Thomas, S. D. Glaser, and R. M. Nadeau (2012). Fault healing promotes high-frequency earthquakes in laboratory experiments and on natural faults, *Nature* **491**, doi: [10.1038/nature11512](https://doi.org/10.1038/nature11512).
- Oth, A., D. Bindi, S. Parolai, and D. Di Giacomo (2011). Spectral analysis of K-NET and KiK-net data in Japan, part II: On attenuation characteristics, source spectra, and site response of borehole and surface stations, *Bull. Seismol. Soc. Am.* **101**, no. 2, 667–687.
- Oth, A., H. Miyake, and D. Bindi (2017). On the relation of earthquake stress drop and ground motion variability, *J. Geophys. Res.* **122**, doi: [10.1002/2017JB014026](https://doi.org/10.1002/2017JB014026).
- Pacor, F., D. Spallarossa, A. Oth, L. Luzi, R. Puglia, L. Cantore, A. Mercuri, M. D'Amico, and D. Bindi (2016). Spectral models for ground motion prediction in the L'Aquila region (central Italy): Evidence for stress-drop dependence on magnitude and depth, *Geophys. J. Int.* **204**, 697–718.
- Peng, Z., and Y. Ben-Zion (2006). Temporal changes of shallow seismic velocity around the Karadere-Düzce branch of the North Anatolian fault and strong ground motion, *Pure Appl. Geophys.* **163**, 567–600, doi: [10.1007/s00024-005-0034-6](https://doi.org/10.1007/s00024-005-0034-6).
- Piña-Valdés, J., A. Socquet, F. Cotton, and S. Specht (2018). Spatio-temporal variations of ground motion in northern Chile before and after the 2014  $M_w$  8.1 Iquique megathrust, *Bull. Seismol. Soc. Am.* **108**, no. 2, 801–814, doi: [10.1785/0120170052](https://doi.org/10.1785/0120170052).
- Purvanche, M. D., and J. G. Anderson (2003). A comprehensive study of the observed spectral decay in strong-motion accelerations recorded in Guerrero, Mexico, *Bull. Seismol. Soc. Am.* **93**, 600–611.
- R Development Core Team (2008). *R: A Language and Environment for Statistical Computing*, R Foundation for Statistical Computing, Vienna, Austria, ISBN: 3-900051-07-0.
- Scuderi, M. M., C. Marone, E. Tinti, G. Di Stefano, and C. Collettini (2016). Precursory changes in seismic velocity for the spectrum of earthquake failure modes, *Nature Geosci.* **9**, 695–700.
- Soldati, G., L. Zaccarelli, L. Faenza, and A. Michelini (2015). Monitoring of crustal seismic velocity variations in the L'Aquila fault zone inferred from noise cross-correlation, *Geophys. J. Int.* **202**, 604–611, doi: [10.1093/gji/ggv172](https://doi.org/10.1093/gji/ggv172).
- Socquet, A., J. Piña-Valdés, J. Jara, F. Cotton, A. Walpersdorf, N. Cotte, S. Specht, F. Ortega-Culuciat, D. Carrizo, and E. Norabuena (2016). An 8-month slow slip event triggers progressive nucleation of the 2014 Chile megathrust, *Geophys. Res. Lett.* **44**, no. 9, 4046–4053, doi: [10.1002/2017GL073023](https://doi.org/10.1002/2017GL073023).
- Trugman, D. T., and P. M. Shearer (2018). Strong correlation between stress drop and peak ground acceleration for recent  $M$  1–4 earthquakes in the San Francisco Bay area, *Bull. Seismol. Soc. Am.* **108**, no. 2, 929–945, doi: [10.1785/0120170245](https://doi.org/10.1785/0120170245).
- Valoroso, L., L. Chiaralucente, R. Di Stefano, and G. Monachesi (2017). Mixed-mode slip behavior of the Altotiberina low-angle normal fault system (Northern Apennines, Italy) through high-resolution earthquake locations and repeating events, *J. Geophys. Res.* **122**, 10,220–10,240, doi: [10.1002/2017JB014607](https://doi.org/10.1002/2017JB014607).
- Wessel, P., and W. H. F. Smith (1991). Free software helps map and display data, *Eos Trans. AGU* **72**, no. 41, 441, 445–446.
- Wickham, H. (2009). *ggplot2: Elegant Graphics for Data Analysis*, Springer-Verlag, New York, New York, ISBN: 978-0-387-98140-6.
- Wooddell, K. E., and N. A. Abrahamson (2014). Classification of main shocks and aftershocks in the NGA-West2 database, *Earthq. Spectra* **30**, 1257–1267.
- Wu, Q., and M. Chapman (2017). Stress-drop estimates and source scaling of the 2011 Mineral, Virginia, mainshock and aftershocks, *Bull. Seismol. Soc. Am.* **107**, 2703–2720.
- Yoshida, K., T. Saito, Y. Urata, Y. Asano, and A. Hasegawa (2017). Temporal changes in stress drop, frictional strength, and earthquake

size distribution in the 2011 Yamagata-Fukushima, NE Japan, earthquake swarm, caused by fluid migration, *J. Geophys. Res.* **122**, 10,379–10,397, doi: [10.1002/2017JB014334](https://doi.org/10.1002/2017JB014334).

Zeileis, A., C. Kleiber, W. Krämer, and K. Hornik (2003). Testing and dating of structural changes in practice, *Comput. Stat. Data Anal.* **44**, 109–123.

Zeileis, A., F. Leisch, K. Hornik, and C. Kleiber (2002). strucchange: An R package for testing for structural change in linear regression models, *J. Stat. Softw.* **7**, no. 2, 1–38.

University of Genova  
DISTAV  
Viale Benedetto XV 5  
16132 Genoa  
Italy  
daniele@dipteris.unige.it  
(D.S.)

German Research Centre for Geosciences GFZ  
Telegrafenberg  
Helmholtzstrasse 6  
14467 Potsdam  
Germany  
bindi@gfz-potsdam.de  
fcotton@gfz-potsdam.de  
rivalta@gfz-potsdam.de  
(D.B., F.C., E.R.)

University Federico II  
Via Cintia  
80126 Naples  
Italy  
matteo.picozzi@unina.it  
(M.P.)

Manuscript received 15 March 2018;  
Published Online 3 July 2018